

Effects of Rapid Intramolecular Electron Transfer on Vibrational Spectra

Tasuku Ito,* Tomohiko Hamaguchi, Haruko Nagino, Tadashi Yamaguchi, John Washington, Clifford P. Kubiak*

Single-electron reductions of linked triruthenium clusters of the general type Ru_3 -pyrazine- Ru_3 produced mixed valence systems showing spectroscopic characteristics of rapid intramolecular electron transfer. Reflectance infrared spectroelectrochemistry was used to characterize the vibrational spectra of mixed valence systems that contained one carbon monoxide ligand on each Ru_3 cluster. Infrared spectra in the CO stretching region showed two resolved, partially coalesced, and coalesced $\nu(\text{CO})$ bands for clusters with rate constants for intramolecular electron transfer k_e increasing from $1 \times 10^9 \text{ s}^{-1}$ up to 5×10^{11} and $9 \times 10^{11} \text{ s}^{-1}$, respectively. These data provide a strong correlation between rates of intramolecular electron transfer and infrared spectral bandshape.

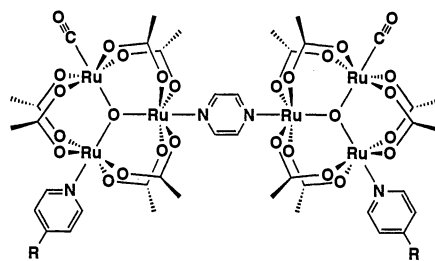
Single-electron transfers are the simplest chemical reactions and are fundamentally important in biology (photosynthesis and respiration) and technology (photography, electrophotography, and solar energy conversion) (1–3). The fastest electron transfers involve the transfer of charge from an electron-donor site to an electron-acceptor site within the same molecule. The Creutz-Taube ion, $[(\text{NH}_3)_5\text{Ru-pyrazine-Ru}(\text{NH}_3)_5]^{5+}$, is a now classical example of an intramolecular charge-transfer complex (4–6). Rather than being viewed as a localized valence ($\text{Ru}^{\text{II}}/\text{Ru}^{\text{III}}$) state, it is generally accepted that charge is delocalized over the complex (5, 6). The semiclassical expression for the rate constant for intramolecular electron transfer k_e in a symmetric charge-transfer complex with no net free energy change ($\Delta G^\circ = 0$) is given by

$$k_e = \kappa \nu_n \times \exp[-(\Delta G_\lambda^* - H_{AB} + H_{AB}^2/4\Delta G_\lambda^*)/RT] \quad (1)$$

where κ is the adiabaticity factor (unity for adiabatic reactions), ν_n is the nuclear frequency factor, which includes both the solvent dielectric response frequency and bond-length/bond-angle reorganizations required by charge transfer between the localized valence states, ΔG_λ^* is the reorganizational energy barrier, and H_{AB} is the electronic coupling between the metal centers (6–8). Thus, the theoretical maximum rate constant for an intramolecular electron transfer can approach the nuclear frequency factor ν_n (10^{12} to 10^{13} s^{-1}) for barrierless ($H_{AB} = 2\Delta G_\lambda^*$) electron transfer. We

show that the rates of intramolecular electron transfer in a series of pyrazine-bridged assemblies of ruthenium clusters can be varied over orders of magnitude by moderating the electronic coupling H_{AB} through ancillary ligand variation. In the most rapidly exchanging systems, electron transfer dynamical effects were observed in the infrared (IR) vibrational spectra.

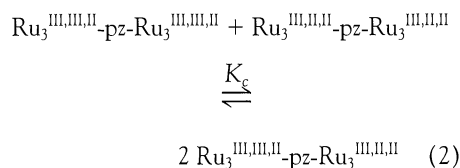
The pyrazine-bridged ruthenium clusters $\text{Ru}_3(\mu_3\text{-O})(\mu\text{-CH}_3\text{CO}_2)_6(\text{CO})(\text{L})(\mu_2\text{-pz}) \text{Ru}_3(\mu_3\text{-O})(\mu\text{-CH}_3\text{CO}_2)_6(\text{CO})(\text{L})$ [pz = pyrazine; L = 4-dimethylaminopyridine (dmap, 1), pyridine (py, 2), and 4-cyanopyridine (cpy, 3) (see scheme below)], which are analogous to those reported by Meyer *et al.* (9), have been synthesized and structurally characterized (10, 11). Each trinuclear Ru_3 unit formally contains one $\text{Ru}(\text{II})$ and two $\text{Ru}(\text{III})$ centers. Clusters 1 through 3 also exhibit characteristic carbon-oxygen stretching absorption [$\nu(\text{CO})$] bands in their infrared spectra that allow changes in the electronic environment of each Ru_3 cluster to be assessed.



1: R = N(CH₃)₂; (L = dmap)
2: R = H; (L = py)
3: R = CN; (L = cpy)

The cyclic voltammograms of clusters 1 through 3 each show four reversible redox waves (Fig. 1). These are characterized by the half-wave potentials for the different redox processes, $E_{1/2}(\text{red/ox})$, referenced versus a saturated sodium chloride calomel electrode (SSCE). Reversible two-electron

oxidation waves were observed at approximately $E_{1/2}(0/+2) = +0.50$ and $E_{1/2}(+2/+4) = +1.3 \text{ V}$ versus SSCE (9, 10, 12). Here, the overall charges of the complexes are expressed in parentheses. Each of the complexes 1 through 3 displays two single-electron reduction waves that correspond formally to $\text{Ru}_3^{\text{III,III,II}}\text{-pz-Ru}_3^{\text{III,III,II}}/\text{Ru}_3^{\text{III,III,II}}\text{-pz-Ru}_3^{\text{III,III,II}}$ (0/–1 overall charge) and then $\text{Ru}_3^{\text{III,III,II}}\text{-pz-Ru}_3^{\text{III,III,II}}/\text{Ru}_3^{\text{III,III,II}}\text{-pz-Ru}_3^{\text{III,III,II}}$ (–1/–2 overall charge) (Fig. 1). The magnitude of splitting between the single-electron (0/–1) and (–1/–2) reduction waves of complex 1 ($\Delta E = 440 \text{ mV}$) corresponds to a comproportionation constant (K_c) (13) of 2.7×10^7 (Eq. 2). The large K_c value is a direct measure of the thermodynamic stability resulting from electronic exchange in the mixed valence state of complex 1 (5). The relationship between the electrochemical value of ΔE and the electronic coupling H_{AB} has been discussed (5, 14–16).



As the adjustable pyridine ligand in the series is changed from 4-dimethylaminopyridine in 1 to an unsubstituted pyridine for 2 and then to an electron-withdrawing 4-cyanopyridine for 3, the values of ΔE and K_c decrease considerably (Table 1); K_c falls

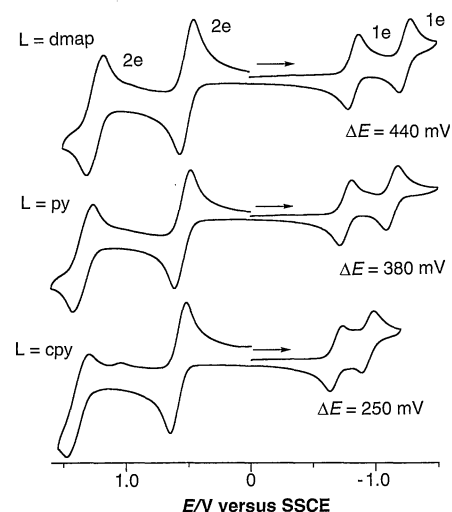


Fig. 1. Cyclic voltammograms are shown for complexes 1 (top), 2 (middle), and 3 (bottom), with methylene chloride as solvent, 0.1 M tetra-*n*-butyl ammonium hexafluorophosphate as supporting electrolyte, and potentials referenced to an SSCE. ΔE is the difference between the half-wave potentials for the two one-electron reduction waves corresponding to the redox processes: $\text{Ru}_3^{\text{III,III,II}}\text{-pz-Ru}_3^{\text{III,III,II}}/\text{Ru}_3^{\text{III,III,II}}\text{-pz-Ru}_3^{\text{III,III,II}}$ (0/–1) and then $\text{Ru}_3^{\text{III,III,II}}\text{-pz-Ru}_3^{\text{III,III,II}}/\text{Ru}_3^{\text{III,III,II}}\text{-pz-Ru}_3^{\text{III,III,II}}$ (–1/–2).

T. Ito, T. Hamaguchi, H. Nagino, T. Yamaguchi, Department of Chemistry, Tohoku University, Aoba, Aramaki, Aoba-ku, Sendai 980-77, Japan.

J. Washington and C. P. Kubiak, Department of Chemistry, Purdue University, West Lafayette, IN 47907-1393, USA.

*To whom correspondence should be addressed. E-mail: ito@agnus.chem.tohoku.ac.jp and cliff@cv3.chem.purdue.edu

Table 1. Electrochemical data for $[\text{Ru}_3(\mu_3\text{-O})(\mu\text{-CH}_3\text{CO}_2)_6(\text{CO})(\text{L})_2(\mu_2\text{-pz})]$ species.

Cluster	L	$E_{1/2}(0/-1)^*$	$E_{1/2}(-1/-2)^*$	ΔE (mV)	K_c
1	dmap	-0.89	-1.33	440	2.7×10^7
2	py	-0.81	-1.19	380	2.7×10^6
3	cpy	-0.68	-0.93	250	1.7×10^4

*Cyclic voltammograms were recorded in 0.1 M tetra-*n*-butyl ammonium hexafluorophosphate in methylene chloride, with voltage versus an SSCE.

Table 2. Summary of electronic spectral data for the ICT bands of mixed valence (-1) state of $\{[\text{Ru}_3(\mu_3\text{-O})(\mu\text{-CH}_3\text{CO}_2)_6(\text{CO})(\text{L})_2(\mu_2\text{-pz})]^{1-}\}$. Data were recorded at -10°C .

Cluster	L	$\tilde{\nu}_{\text{max}}$ (cm^{-1})	ϵ_{max} ($\text{M}^{-1}\text{cm}^{-1}$)	$\Delta\tilde{\nu}_{1/2}$ (cm^{-1})	H_{AB} (cm^{-1}) [*]
1	dmap	12,100	12,200	3760	2180
2	py	11,800	10,700	3930	2060
3	cpy	10,800	6610	5220	1310

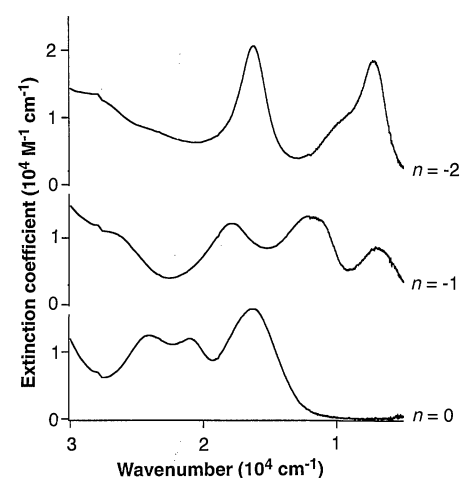
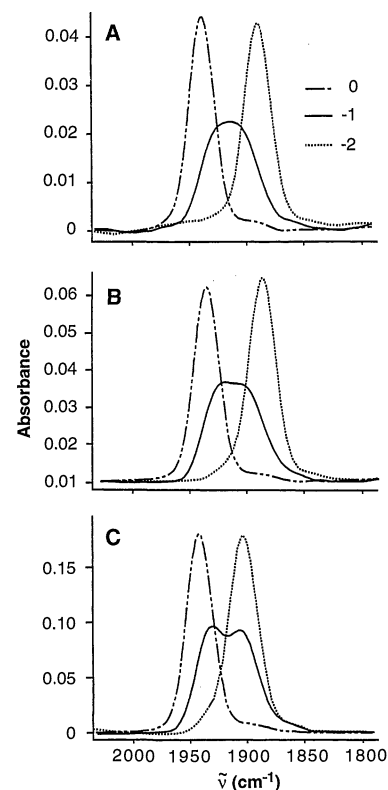
* $H_{\text{AB}} = 2.05 \times 10^{-2} (\tilde{\nu}_{\text{max}} \epsilon_{\text{max}} \Delta\tilde{\nu}_{1/2})^{1/2} / r$ (7), where r is the weighted average intercluster Ru...Ru separation from the crystal structure of 1 (17).

by three orders of magnitude to 1.7×10^4 for complex 3. It is evident that the magnitude of the electronic coupling H_{AB} can be moderated over a large range by a relatively simple ligand substitution in the series 1 through 3. Remote ligand control of electronic coupling in mixed-valence complexes is not unusual (15–17). However, to our knowledge, the wide variation seen in 1 through 3 has not been reported previously. In the present case, it appears that two conditions are simultaneously met: (i) very favorable overlap between the Ru_3 cluster d -electron system and the bridging pyrazine π^* system and (ii) the ability to raise or lower Ru_3 cluster d -electron levels engaging the pyrazine π^* system by changing the electron donor or acceptor nature of the

adjustable pyridine ligand (18).

H_{AB} is usually determined by characterization of the intervalence charge transfer (ICT) band as explained by Hush (7). The electronic absorption spectra were obtained in the isolated neutral (0), mixed valence (-1), and fully reduced (-2) states (Fig. 2) (19). The mixed valence states of clusters 1 through 3 all exhibited intense ICT bands in the region of 12,100 cm^{-1} (1) to 10,800 cm^{-1} (3). No bands in this region of the electronic spectra were observed in the isolated (0) state or the fully reduced (-2) states. Values of absorption band maxima ($\tilde{\nu}_{\text{max}}$), molar extinction coefficients (ϵ_{max}), and absorption band half-widths ($\Delta\tilde{\nu}_{1/2}$) derived from the spectral deconvolution of 1 through 3 and metrical parameters from the crystal structure of 1 were used to estimate H_{AB} (Table 2). Estimates of H_{AB} , derived from optical data of the singly reduced (-1) charge-transfer states, ranged by nearly a factor of 2 from 2180 cm^{-1} (1) to 1310 cm^{-1} (3). In the Robin-Day classification of intervalence charge-transfer complexes (20), cluster 3 can be considered to be a largely charge-localized class II complex, on the basis of $\Delta\tilde{\nu}_{1/2}$. By making typical assumptions ($\kappa = 1$, $\nu_n = 5 \times 10^{12} \text{ s}^{-1}$, and $\Delta G_\lambda^* = \tilde{\nu}_{\text{max}}/4$) (6), Eq. 1 then predicts a rate constant for intramolecular electron transfer $k_e = 1 \times 10^9 \text{ s}^{-1}$ at 263 K for 3. The high degree of electronic coupling for 1 and 2 suggests that these complexes are approaching delocalized class III behavior, where a semiclassical description (8) is no longer applicable, but where rates of electron transfer are expected to be exceptionally fast (21).

The vibrational spectra of the complexes 1 through 3 were obtained by using reflectance IR spectroelectrochemistry (SEC). The spectroelectrochemical cell used in this

**Fig. 2.** Electronic absorption spectral data are shown for complex 1 in the neutral isolated ($n = 0$; bottom), one-electron reduced ($n = -1$; middle), and two-electron reduced ($n = -2$; top) states, with methylene chloride as solvent and a temperature of -10°C .**Fig. 3.** IR spectra are shown for $\{[\text{Ru}_3(\mu_3\text{-O})(\mu\text{-CH}_3\text{CO}_2)_6(\text{CO})(\text{L})_2(\mu_2\text{-pz})]^n\}$ [$n = 0$ (---), -1 (—), and -2 (···)] in 0.1 M tetra-*n*-butyl ammonium hexafluorophosphate methylene chloride solution for (A) L = dmap, 1; (B) L = py, 2; (C) L = cpy, 3.

study has been reported previously (22, 23). Controlled potentials were applied to prepare the singly (-1) and doubly (-2) reduced states of clusters 1 through 3 for IR spectroscopic observation. In the isolated (0) state, complex 1 exhibits a single $\nu(\text{CO})$ band at 1938 cm^{-1} (Fig. 3A). The normal modes associated with C-O stretching of the carbon monoxide ligands on each $\text{Ru}_3^{\text{III,III,II}}$ unit have identical frequencies because of their identical local environments and large spatial separation. The doubly reduced species also gives rise to a single $\nu(\text{CO})$ band, but at 1889 cm^{-1} , reflecting identical redox states at each $\text{Ru}_3^{\text{III,II,II}}$ cluster. In view of these results, it is reasonable to expect that the single-electron reduced state of 1 will show two $\nu(\text{CO})$ bands, one characteristic of a $\text{Ru}_3^{\text{III,III,II}}$ environment and the other characteristic of $\text{Ru}_3^{\text{III,II,II}}$. However, for the singly reduced form of 1, two $\nu(\text{CO})$ bands are not observed. Rather, a broad absorption band at the average energy of the bands observed for the isolated (0) and doubly reduced (-2) states of 1 is seen (Fig. 3A). The degree of “coalescence” of the IR spectra depends on the degree of electronic coupling between the pyrazine-linked Ru_3 clusters (Fig. 3). As H_{AB} decreases from

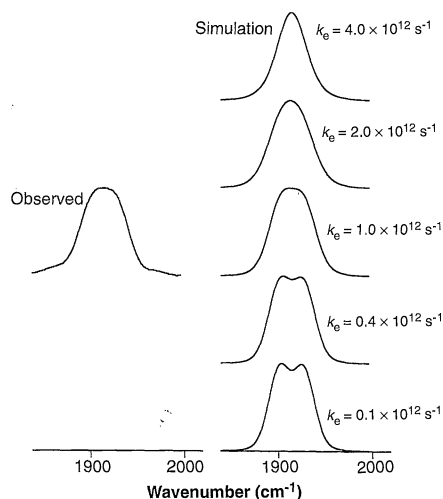


Fig. 4. Comparison of observed to simulated (41) IR spectra for the mixed valence state of **1** as a function of the intramolecular electron transfer rate constant k_e .

2180 cm^{-1} for **1** to 1310 cm^{-1} for **3**, two distinct $\nu(\text{CO})$ bands at 1931 cm^{-1} and 1904 cm^{-1} become resolved. Cluster **2** with an intermediate value of H_{AB} (2060 cm^{-1}) shows an intermediate degree of spectral coalescence in the singly reduced state.

The dependence of IR absorption bandshape on electronic coupling in the mixed valence states (H_{AB}) is consistent with extremely rapid intramolecular electron transfer. The question of how to accurately determine electron transfer rate constants from IR spectroscopic measurements is less clear at this time. Carbonyl ligand exchange in $\text{Fe}(\text{CO})_3(\eta^4\text{-norbornadiene})$ was reported to be on the order of $k_{\text{ex}} = 10^{12} \text{ s}^{-1}$ at 24°C, as calculated from the observed coalescence of two IR bands as a function of temperature (24). Grevels *et al.* assumed a multiple-well potential-energy surface for the process and assumed that the dynamics could be treated in a manner similar to that routinely applied to nuclear magnetic resonance (NMR) spectroscopy (Bloch equations) (24). This effect was subsequently explained as resulting from torsional modulation of the vibrational coupling (single potential-energy well) between two $\nu(\text{CO})$ modes (25), but certain features of the coalescing IR spectra may be explained only by the multiple well (exchange) model (26). Other systems reported to show dynamical effects in their IR spectra involve conformational changes or rapid proton exchange reactions (27–30). Unusual features in the IR spectra of organic dicarbonyl radical anions have been ascribed to purely vibronic transitions (31, 32). In several isolated cases, intramolecular electron exchange has been invoked to explain apparent coalescence of IR spectral features in ICT complexes (33–38). It has also been

shown that dynamic processes wholly different from equilibration of dissimilar chemical environments can produce vibrational spectra that appear coalesced, but intramolecular electron transfers were not considered (25, 39, 40). Intramolecular electron transfers can be sufficiently fast that lifetime broadening of IR spectra would be expected. However, a continuous correlation of vibrational spectral lineshape with electron transfer dynamics has not been reported previously.

Rate constants for intramolecular electron transfer were estimated, assuming a model where the Bloch equations apply (26, 41). In NMR spectroscopy, dynamic processes occurring on a millisecond time scale can produce spectral broadening and coalescence. To observe any line broadening in the IR spectrum due to a dynamical effect, we assumed that the process must occur on a time scale shorter than 10 ps (rate constant of 10^{11} s^{-1}). Complex **1** shows this fast exchange behavior, but complex **3** does not. Equation 1 predicts a rate constant for **3** of $1 \times 10^9 \text{ s}^{-1}$. This is well below the threshold for observation by IR spectroscopy. The spectrum of cluster **3** (Fig. 3C) can then safely be assumed to show no line broadening arising from electron exchange. The bands at 1931 and 1905 cm^{-1} in the spectrum of **3** in the (–1) state represent the “stopped exchange” limit on the IR spectroscopy scale. We then simulated changes in IR line shape due to electron exchange dynamics (41). Figure 4 shows a comparison of the simulated spectral line shape as a function of k_e to the observed spectrum for complex **1**. The rates of electron transfer estimated for **1** and **2** are $9 \pm 3 \times 10^{11}$ and $5 \pm 3 \times 10^{11} \text{ s}^{-1}$. Uncertainties in the rates of electron transfer are present but the rate constants obtained for **1** through **3** are reasonable within the context of theories of electron transfer. The correlation of IR line shape for the mixed valence states of **1** through **3** with electronic coupling H_{AB} provides convincing evidence of the effects of intramolecular electron transfer on the time scale of observation by IR spectroscopy ($<10^{-11} \text{ s}$).

REFERENCES AND NOTES

- G. L. Closs, M. D. Johnson, J. R. Miller, P. Piotrowski, *J. Am. Chem. Soc.* **111**, 3751 (1989).
- J. R. Winkler and H. B. Gray, *Chem. Rev.* **92**, 369 (1992).
- D. Astruc, *Electron Transfer and Radical Processes in Transition-Metal Chemistry* (VCH, Weinheim, Germany, 1995).
- C. Creutz and H. Taube, *J. Am. Chem. Soc.* **91**, 3988 (1969).
- D. E. Richardson and H. Taube, *Coord. Chem. Rev.* **60**, 107 (1984).
- C. Creutz, *Prog. Inorg. Chem.* **30**, 1 (1983).
- N. S. Hush, *ibid.* **8**, 391 (1967).
- N. Sutin, *ibid.* **30**, 441 (1983).
- J. A. Baumann, D. J. Salmon, S. T. Wilson, T. J. Meyer, *Inorg. Chem.* **18**, 2472 (1979).
- H. Nagino, thesis, Tohoku University, Sendai, Japan (1995).
- Preparation of complexes **1** through **3**. A mixture of $\text{Ru}_3(\mu_3\text{-O})(\mu\text{-CH}_3\text{CO}_2)_6(\text{CO})(\text{dmap})(\text{H}_2\text{O})$ (50 mg; 0.059 mmol) and $\text{Ru}_3(\mu_3\text{-O})(\mu\text{-CH}_3\text{CO}_2)_6(\text{CO})(\text{dmap})(\text{pz})$ (54 mg; 0.059 mmol) in CH_2Cl_2 (5 ml) was stirred for 14.5 hours at room temperature. The resulting solution was chromatographed over silica gel (Wakogel C-200; column length, 18 cm; column diameter, 2.5 cm) with $\text{CH}_2\text{Cl}_2/\text{CH}_3\text{OH}$ 100:0.7 (v/v) as the eluting agent. The compound was isolated from the first blue-green main band. Yield was 54 mg. Analysis: Calculated for $\text{Ru}_6\text{C}_{44}\text{H}_{60}\text{O}_{28}\text{N}_6$: C, 30.59%; H, 3.50%; N, 4.87%. Found: C, 30.96%; H, 3.75%; N, 4.66%. Fast atom bombardment mass spectrometry (FABMS): mass/charge ratio (m/z) 1727 [calculated molecular weight (M) = 1727], 1698 [calcd ($M\text{-CO}$) = 1699], and 1672 [calcd ($M\text{-CO}_2$) = 1672]. $^1\text{H NMR}$ (270 MHz, CDCl_3) was 9.30 (4H, pz), 8.95 (4H, dmap-o), 7.24 (4H, dmap-m), 3.34 (12H, dmap CH_3), 2.25 (12H, acetate CH_3), 2.12 (12H, acetate CH_2), and 1.95 (12H, acetate CH_3) ppm. Complex **1** was also characterized by x-ray crystallography. Details are available elsewhere. Complexes **2** and **3** were prepared similarly from the appropriate *para*-substituted pyridine complexes. Analysis of **2**: Calculated for $\text{Ru}_6\text{C}_{40}\text{H}_{50}\text{O}_{28}\text{N}_4\text{-0.5C}_2\text{H}_4$: C, 30.66%; H, 3.41%; N, 3.33%. Found: C, 30.57%; H, 3.25%; N, 3.66%. FABMS: m/z 1647 (calcd M = 1641). $^1\text{H NMR}$ (270 MHz, CDCl_3) was 9.23 (4H, pz), 8.95 (4H, py-o), 8.13 (2H, py-p), 8.05 (4H, py-m), 2.24 (12H, acetate CH_3), 2.15 (12H, acetate CH_2), and 1.99 (12H, acetate CH_3) ppm. Analysis of **3**: Calculated for $\text{Ru}_6\text{C}_{42}\text{H}_{48}\text{O}_{28}\text{N}_6$: C, 28.90%; H, 3.12%; N, 4.82%. Found: C, 28.85%; H, 2.95%; N, 4.78%. FABMS: m/z 1662 [calcd ($M\text{-CO}$) = 1663], 1635 [calcd ($M\text{-CO}_2$) = 1635]. $^1\text{H NMR}$ (270 MHz, CDCl_3) 9.08 (4H, pz), 8.75 (4H, cpy), 8.22 (4H, cpy), 2.25 (12H, acetate CH_2), 2.20 (12H, acetate CH_3), and 2.03 (12H, acetate CH_3) ppm.
- M. Abe *et al.*, *Inorg. Chem.* **35**, 6724 (1996).
- The comproportionation constant, K_c , is calculated from the Nernst equation in the form: $\exp(\Delta E_{1/2}/25.69)$, where $\Delta E_{1/2}$ corresponds to the difference measured by cyclic voltammetry of the half-wave potentials for the first and second reductions in millivolts (5).
- J. E. Sutton and H. Taube, *Inorg. Chem.* **20**, 3125 (1981).
- R. de la Rosa, P. J. Chang, F. Salaymeh, J. C. Curtis, *ibid.* **24**, 4229 (1985).
- Y. Dong and J. T. Hupp, *ibid.* **31**, 3170 (1992).
- M. Lacoste *et al.*, *J. Am. Chem. Soc.* **112**, 9548 (1990).
- The relevant Ru d level is closer to the pyrazine π^* level in **1** than it is in **3**. This is supported by the following two facts: (i) the metal-to-ligand charge transfer (MLCT) electronic absorption bands for the Ru- d to pyrazine π^* transition appear at 482 nm in **1**, 475 nm (overlapped) in **2**, and 450 nm (overlapped) in **3**; and (ii) the reduction potentials become more positive from **1** to **3** (Table 1).
- The lowest energy electronic absorption bands of **1** in the mixed valence (–1) state at 7100 cm^{-1} are assigned to intra- Ru_3 cluster transitions, because the fully reduced (–2) species exhibits a broad band at nearly the same energy with double the intensity. Significantly, the singly reduced but nonbridged species $[\text{Ru}_3^{\text{III,II,II}}(\mu_3\text{-O})(\mu\text{-CH}_3\text{CO}_2)_6(\text{CO})(\text{dmap})_2]^-$ shows an absorption band similar to that observed at 7100 cm^{-1} for **1** in the fully reduced (–2) state.
- M. B. Robin and P. Day, *Adv. Inorg. Chem. Radiochem.* **10**, 247 (1967).
- According to a Hush treatment of intervalence charge transfer bands (6), the expected half widths of the intervalence charge transfer (ICT) band in the mixed valence (–1) states are $\Delta \nu_{1/2}(\text{calc.}) = 5290 \text{ cm}^{-1}$ for **1**, 5220 cm^{-1} for **2**, and 4990 cm^{-1} for **3**. Comparison of these values with the experimentally observed data (Table 2) indicates that **1** and **2** are close to fulfilling Robin-Day (20) class III (delocalized) behavior, whereas **3** is clearly class II.
- IR spectral changes accompanying thin-layer bulk electrolysises were measured with a flow-through spectroelectrochemical cell. Spectroelectrochemical experiments were carried out in 0.1 M tetra-*n*-butyl ammoni-

- um hexafluorophosphate solutions, using freshly distilled tetrahydrofuran or methylene chloride. All solutions were prepared under an atmosphere of nitrogen and degassed completely before injection into the SEC cell. Blank reference solutions containing 0.1 M tetra-*n*-butyl ammonium hexafluorophosphate were used for the Fourier transform IR solvent subtractions. A Princeton Applied Research (PAR) model 175 Universal Programmer with a PAR model 176 Current Follower were used to effect and monitor thin-layer bulk electrolyses. The IR spectra were acquired with a Mattson Research Series Fourier transform IR equipped with a MCT (mercury-cadmium-telluride) detector.
23. R. E. Wittrig and C. P. Kubiak, *J. Electroanal. Chem.* **393**, 75 (1995).
 24. F.-W. Grevels et al., *Angew. Chem. Int. Ed. Engl.* **26**, 885 (1987).
 25. H. L. Strauss, *J. Am. Chem. Soc.* **114**, 905 (1992).
 26. J. J. Turner, C. M. Gordon, S. M. Howdle, *J. Phys. Chem.* **99**, 17532 (1995).
 27. M. Eigen, *Angew. Chem. Int. Ed. Engl.* **3**, 1 (1964).
 28. B. Cohen and S. Weiss, *J. Phys. Chem.* **87**, 3606 (1983).
 29. R. A. MacPhail and H. L. Strauss, *J. Chem. Phys.* **82**, 1156 (1985).
 30. S. Bratos, G. Tarjus, P. Viot, *ibid.* **85**, 803 (1986).
 31. S. Mazur, C. Sreekumar, A. H. Schroeder, *J. Am. Chem. Soc.* **98**, 6713 (1976).
 32. A. H. Schroeder and S. Mazur, *ibid.* **100**, 7339 (1978).
 33. G. M. Tom and H. Taube, *ibid.* **97**, 5310 (1975).
 34. F. Coat and C. Lapinte, *Organometallics* **15**, 477 (1996).
 35. R. H. Magnuson and H. Taube, *J. Am. Chem. Soc.* **94**, 7213 (1972).
 36. H. Krentzien and H. Taube, *ibid.* **98**, 6379 (1976).
 37. M. B. Sponzler, *Organometallics* **14**, 1920 (1995).
 38. R. Wu et al., *J. Chem. Soc. Chem. Commun.* **1994**, 1657 (1994).
 39. K. A. Wood and H. L. Strauss, *J. Phys. Chem.* **94**, 5677 (1990).
 40. A. E. Johnson and A. B. Meyers, *ibid.* **100**, 7778 (1996).
 41. IR spectral lineshapes were simulated with the dynamical simulation program VIBEXGL: Program for the Simulation of IR Spectra of Exchanging Systems, made available by R. E. D. McClung, University of Alberta, Alberta, Canada.
 42. Supported by NSF grants (CHE-9319173 and CHE-9615886) to C.P.K. and Grants-in-Aid for Scientific Research (08243214 and 09874128) from the Ministry of Education, Science, and Culture and by a grant from Monbusho International Scientific Research Program (No. 09044054) (Japan) to T.I. We also gratefully acknowledge the Japan Society for the Promotion of Science for fellowship support to C.P.K. and Natural Sciences and Engineering Research Council (Canada) for a postdoctoral fellowship to J.W.

25 March 1997; accepted 9 June 1997

An Advective-Reflective Conceptual Model for the Oscillatory Nature of the ENSO

J. Picaut,* F. Masia, Y. du Penhoat†

Recent findings about zonal displacements of the Pacific warm pool required a notable modification of the delayed action oscillator theory, the current leading theory for the El Niño–Southern Oscillation (ENSO). Simulations with a linearized coupled ocean-atmosphere model resulted in 3- to 6-year ENSO-like oscillations, with many of the variable model parameters found to be very close to their observed values. This simple model suggests that ocean processes that are ignored or underestimated in the delayed action oscillator theory, such as zonal current convergence, zonal advection of sea surface temperature, and equatorial wave reflection from the eastern ocean boundary, are fundamental to the development of the ENSO, in particular to its manifestations in the central equatorial Pacific.

Earth climate variations on interannual time scales are dominated by a coupled ocean-atmosphere interaction in the Pacific. This interaction connects a large-scale oceanic sea surface temperature (SST) anomaly of the tropical Pacific (El Niño) to the large-scale atmospheric Southern Oscillation, which is characterized by a sea-level pressure seesaw between French Polynesia and north Australia [defined by the Southern Oscillation Index (SOI)]. This coupled phenomenon, named the ENSO, oscillates irregularly

(roughly every 4 years) into a warm phase and a cold phase (Fig. 1). The warm phase, El Niño, is characterized by warm SST and weak easterly winds in the central and eastern equatorial Pacific, energetic westerly winds in the western Pacific, and negative SOI; whereas the cold phase, La Niña, is characterized by cold SST and strong easterly winds in the central and eastern equatorial Pacific, weak westerly winds in the western Pacific, and positive SOI. The gross features of the ENSO, and some of its dramatic climatic impacts, can be predicted 6 months to a year in advance by dynamical coupled ocean-atmosphere models (1–3). However, the prediction skills of these models are still limited by our insufficient understanding of the intrinsic mechanism that is responsible for the ENSO.

Bjerknes (4) proposed that the ENSO

is a self-sustained system in which SST variations in the eastern and central equatorial Pacific produce wind variations, which in turn produce SST changes. However, this scenario leads to a never ending warm or cold state. A mechanism for the oscillatory nature of the ENSO was originally proposed by McCreary (5), based on the reflection of a subtropical oceanic upwelling Rossby wave against the western ocean boundary. Battisti, Hirst, Schopf, and Suarez (6–8) proposed a concept that was similar to McCreary's (but was better supported by observations and equatorial wave theory), known as the delayed action oscillator, in which equatorial Rossby waves reflected as upwelling equatorial Kelvin waves are essential (9). Given the 9-month total travel time of the equatorial upwelling Rossby and reflected Kelvin waves, this concept asserts that it is the continuous arrival of upwelling Kelvin waves that slowly erodes the growing SST-wind interaction in the eastern equatorial Pacific, finally stops it after 1 or 2 years, and eventually turns the El Niño event into a La Niña event.

The delayed action oscillator theory is currently the leading theory for the ENSO, although it has several flaws. First, the maxima in the coupled SST–wind stress fields, simulated by the different models that led to this theory, are located 20° to 40° too far into the eastern equatorial Pacific as compared with observations (Fig. 1) (10). Second, on the basis of mooring data all along the equatorial Pacific and satellite altimetry data, several authors have questioned the effectiveness of the western ocean boundary as an equatorial wave reflector (11–14). In contrast, it seems that equatorial Kelvin waves reflect quite well on the eastern boundary as equatorial Rossby waves (14). Third, the models that have led to this theory of the ENSO are based on the dominant role of thermocline displacements on SST in the eastern equatorial Pacific, and they underestimate or misinterpret the effects of zonal advection (15). As a result, these models consider the eastern equatorial Pacific (where ENSO-related SST variations are the strongest) to be the source of the ENSO air-sea interaction, instead of the central equatorial Pacific (Fig. 1) (10).

The central equatorial Pacific has been confirmed as the source of the ENSO in recent studies (16–19), which indicated that the central equatorial Pacific SST varies between 26° and 30°C, predominantly on the ENSO time scale, as a result of the strong eastward and westward displacements of the eastern edge of the western Pacific warm pool. Because the SST varies around the approximate 28°C

Groupe SURTROPAC, L'Institut Français de Recherche Scientifique pour le Développement en Coopération-ORSTOM, BP A5, 98848, Nouméa, New Caledonia.

*To whom correspondence should be addressed. E-mail: picaut@noumea.orstom.nc

†Present address: Groupe de Recherche en Géodésie Spatiale, 14 avenue Edouard Belin, 31401, Toulouse, France.